1993

Limits to Cosmic Background Fluctuations at 8.44 GHz between Angular Scales 10^2 to 200^2

E. B. Fomalont

Bruce Partridge
Haverford College, bpartrid@haverford.edu

James D. Lowenthal

Rogier A. Windhorst

1993

Limits to Cosmic Background Fluctuations at 8.44 GHz between Angular Scales 10^2 to 200^2

Edward B. Fomalont

R. Bruce Partridge
Haverford College

James D. Lowenthal

Rogier A. Windhorst

THE ASTROPHYSICAL JOURNAL, 404:8–20, 1993 February 10

LIMITS TO COSMIC BACKGROUND RADIATION FLUCTUATIONS AT 8.44 GHz BETWEEN ANGULAR SCALES 10″ AND 200″

EDWARD B. FOMALONT
National Radio Astronomy Observatory,[1] Edgemont Road, Charlottesville, VA 22903-2475
R. BRUCE PARTRIDGE
Haverford College, Department of Astronomy, Haverford, PA 19041
JAMES D. LOWENTHAL[2]
Steward Observatory, University of Arizona, Tucson, AZ 85721
AND
ROGIER A. WINDHORST[3]
Department of Physics and Astronomy, Arizona State University, Tempe, AZ 85287-1504
Received 1992 June 19; accepted 1992 August 11

ABSTRACT

We have used the VLA at 8.44 GHz to measure fluctuations in the cosmic background radiation (CBR) from two deep images, each 7′ × 7′ in size. No fluctuations between the angular scales 10″ and 200″ were detected. The most accurate limit (95% confidence) is $\Delta T/T_{\rm CBR} < 1.9 \times 10^{-5}$ for 80″ resolution. For random Gaussian fluctuations with coherence angle θ_c, the limits are $\Delta T/T_{\rm CBR} < 3.0 \times 10^{-5}$ for $22'' < \theta_c < 60''$. Outside this range the limits increase to $\Delta T/T_{\rm CBR} < 5 \times 10^{-5}$ at $\theta_c = 12''$ or 100″ and $\Delta T/T_{\rm CBR} < 10 \times 10^{-5}$ at $\theta_c = 5''$ or 120″. Similar limits have been obtained for the *circularly* and *linearly* polarized components of the CBR fluctuations. These limits were derived from the residual fluctuations in the images after (1) removing brighter foreground sources (>14.5 μJy) which covered about 10% of each image; (2) estimating fluctuations of weaker sources by extrapolating the count of $dN/dS = 4.6S^{-2.3}$ Jy^{-1} sr^{-1} to 4 μJy; and (3) determining fluctuations from receiver noise and instrumental errors by comparing the image variances from two independent halves of the data set. All analysis was made on *dirty* images, in which the statistical properties of instrumental and sky fluctuations are well-defined.

Subject headings: cosmic microwave background — polarization

1. GALAXY FORMATION AND CBR FLUCTUATIONS

Fluctuations in the surface brightness of the sky at centimeter wavelengths at high Galactic latitude may be caused by one or more of the following: (1) intrinsic fluctuations in the cosmic microwave background radiation (CBR) introduced around the epoch of decoupling at a redshift $z \approx 1000$; (2) fluctuations in the CBR introduced by a later episode of galaxy or cluster formation; (3) foreground radio sources; and (4) Galactic emission from relativistic particles, ionized hydrogen and dust. The first three mechanisms are of cosmological interest. These four may be distinguished by observations made at different wavelengths and different angular scales.

Intrinsic fluctuations in the CBR that are primordial will produce density or velocity perturbations on the surface of last scattering at a redshift $z \approx 1000$ (see, e.g., Sachs & Wolfe 1967; Kaiser & Silk 1986; Bond & Efstathiou 1987). Because of the finite thickness of that surface, any perturbations on angular scales much less than 10′ are smoothed away. As a consequence, most searches for intrinsic fluctuations in the CBR have been carried out on scales of tens of arcminutes or more (e.g., Meyer, Cheng, & Page 1991; Meinhold & Lubin 1991; Timbie & Wilkinson 1990; Davies et al. 1987). Recently, the *COBE* Differential Microwave Radiometer (DMR) instrument (Smoot et al. 1992) has detected fluctuations with angular scale 10° at a level of $\Delta T/T_{\rm CBR} = (1.1 \pm 0.2) \times 10^{-5}$ and a quadrupole term of about 4×10^{-6}. These fluctuations appear to be scale-invariant, and are consistent with inflationary models and a universe dominated by cold dark matter (Wright et al. 1992; for reviews see Wilkinson 1986; Kaiser & Silk 1986; Bond 1988; Partridge 1988).

Additional fluctuations in the CBR may be introduced at later epochs (i.e., at much lower redshifts) by processes responsible for the formation of galaxies or other large-scale structures. The explosive scenario of Ostriker & Cowie (1981) and Ikeuchi (1981), for instance, will produce rapid motions in the material content of the universe and will ionize some of it. Both motions and ionization result in temperature CBR fluctuations when that radiation interacts with the plasma. The effects on the CBR have been investigated by Ostriker & Vishniac (1986) and treated in more detail by Vishniac (1987). An interesting feature of this scenario of galaxy formation is that the angular spectrum of fluctuations in the CBR is shifted toward smaller angular scales: fluctuations on angular scales below tens of arcminutes are now possible. Other models, such as the "dusty young galaxy" models of Bond, Carr, & Hogan (1991), also predict fluctuations which increase in amplitude as the angular scale decreases. Previous searches for small-scale fluctuations (e.g., by Uson & Wilkinson 1984; Martin & Partridge 1988; Readhead et al. 1989; Fomalont et al. 1988; Myers, Readhead, & Lawrence 1993) and that described in this paper are particularly useful in testing such models.

[1] The National Radio Astronomy Observatory is operated by Associated Universities, Inc., under cooperative agreement with the National Science Foundation.
[2] Currently at Space Telescope Science Institute, 3700 San Martin Drive, Baltimore, MD 21218, and Johns Hopkins University, Department of Physics and Astronomy, Homewood Campus, Baltimore, MD 21218.
[3] Alfred P. Sloan Research Fellow.

Foreground radio sources will also introduce fluctuations into the microwave sky. Detailed modeling by Franceschini et al. (1989) suggests that foreground sources will introduce a typical scatter amplitude corresponding to a fractional CBR fluctuation of $\Delta T/T \approx (3\text{–}6) \times 10^{-5}$ at 8.44 GHz and in the range of angular scale of tens of arcseconds. As we shall see, our ability to detect, catalog, and remove the effects of foreground sources stronger than 14.5 μJy, and to estimate the effect of the weaker sources, substantially improves our limits to CBR fluctuations.

In this paper we describe measurements made at the Very Large Array (VLA) at 8.44 GHz ($\lambda = 3.55$ cm) designed to search for fluctuations in the sky over a range of angular scales from 10″ to 200″. The observations and data reduction are summarized in § 2. The removal of the strong sources is described in § 3. In § 4 we discuss the separation of the residual data set (with the strong sources removed) into two parts in order to determine the various components of the image fluctuations. A tabulation of the image variances is also given. In § 5 we describe the method used to simulate the image variances produced by a plausible density of faint sources. By removing their contribution, we derive accurate limits to fluctuations in the CBR. We also determine limits to the circular and linear polarized component of CBR fluctuations. The discussion of the results and comparison with other CBR observations and with current models are given in § 6. A brief summary and anticipated further observations are given in § 7.

2. OBSERVATIONS AND DATA REDUCTION

2.1. *Observations*

We observed two fields, both known from earlier VLA work (Windhorst et al. 1985; Donnelly, Partridge, & Windhorst 1987; Martin & Partridge 1988) to be free of bright sources, in Cepheus at $\alpha = 03^h10^m00^s$, $\delta = 80°10'00''$, and in Lynx 2 at $\alpha = 08^h41^m40^s$, $\delta = 44°45'00''$ (Windhorst et al. 1985). Both coordinates are at equinox B1950.0. The precise field centers were selected to place the brightest remaining sources in or near the null of the primary beam of the VLA antennas at 8.44 GHz. The field of view, determined by the diameter of the primary beam of the 25 m antennas, is 312″ full width at half-power, 444″ full width to the first nulls.

Our VLA observations at 8.44 GHz have been discussed by Windhorst et al. (1992), and the parts relevant to the current paper will be briefly summarized here. The observations occurred on eight different days in 1989 December and 1990 January with the Very Large Array in the D-configuration. In this configuration, the spacing of the antennas ranged from 40 to 1000 m, and the highest resolution was $\approx$10″ full width at half-power (FWHP). We observed at two frequencies, 8.415 and 8.465 GHz, each with dual circular polarization of 50 MHz bandwidth. All four Stokes parameters were measured. We chose long integrations and high declinations for the field centers to ensure uniform and symmetric coverage of the *u-v* plane. In all, we obtained about 62 hr of integration on the Lynx field, and about 17 hr on the Cepheus field. In addition, in 1988 September we had made preliminary observations of the Cepheus field in poor weather. Only one frequency was available, at which we observed for 23 hr. These earlier data were added to those obtained in 1989–1990, giving us the equivalent of 30 hr of good observations on this field. The observing schedule alternated between a 27 minute source observation and a 3 minute phase-calibrator observation.

2.2. *Editing and Calibration*

The data were edited in several steps. First, data associated with antennas shadowed by other antennas were removed, since corrections for shadowing are not reliable and there is a possibility of cross-talk between the antennas. Next, observations spoiled by infrequent bursts of interference were readily found by inspecting the visibility data, sampled every 20 s, and we discarded all visibility records larger than 8 times the expected rms noise per sample integration, which is about 13 mJy. This value is much larger than the expected signal from the sky. The visibility data were then averaged to 60 s for subsequent imaging. It is known from other deep VLA integrations that a faulty correlator channel can produce a spurious *constant* signal in addition to the stochastic signal from the receivers and the pseudostochastic signal from the sky. Thus, if averaged over several hours, the visibility amplitude from a faulty correlator will be much larger than that expected from the receivers and the sky. About 10 correlators (out of 1404) had such excessive visibility amplitude after averaging, and they were removed from the data base (see Fomalont et al. 1988 for details). In total, less than 5% of the observations were excluded by the above conditions. However, one observation day of 8 hr was completely discarded because snow had collected on the antenna surface, and the sky signal had decreased by more than a factor of 5. This entire day would have been equivalent to only a 20 minute integration at nominal sensitivity.

We based the amplitude calibration of the VLA data on 3C 48 for the Cepheus field, adopting 3.34 and 3.32 Jy for its flux densities in the centers of the two frequency bands at 8.415 and 8.465 GHz, respectively. For the Lynx field we used 3C 286, with flux densities of 5.20 and 5.18 Jy, respectively. These values agree with the flux density scale of Baars et al. (1977). As phase calibrators we observed 0212+735 and 0917+449, which are near the Cepheus and Lynx fields, respectively. Residual variations in the gain of the system after calibration were less than 3%. Residual phase variations were generally less than 10° even for the 1 km baselines. Preliminary radio images were made for each day's data alone in order to search for additional data problems. However, all images were of good quality, with the general noise distribution at the expected level.

The polarization data were calibrated in the standard manner. The instrumental terms (cross-talk between the right-hand and left-hand circular polarization channels) were determined from the observations of the phase calibrators to a level of 1%. The zero point of the electric vector of linear polarization was determined from the 3C 286 and 3C 48 observations to an accuracy of 3°. Both sources have known linear polarization angles at 8.44 GHz (Altschuler & Wardle 1976).

3. THE RADIO IMAGES

3.1. *The Sources in the Radio Fields*

We combined the entire data sets at both frequencies for both the Cepheus and the Lynx field, and images were produced using the standard NRAO software in AIPS. The resulting average frequency was 8.44 GHz. In making the images, the best sensitivity to point sources is obtained if the data points are weighted by the inverse square of their rms noise. The rms noise for each day's data was estimated from the observing time and the system sensitivity, which in turn varied with source elevation and weather conditions.

TABLE 1

IMAGING PARAMETERS

Resolution (1)	Image Size (pixels) (2)	Pixel Separation (3)	Image Size (4)	Data Taper (m) (5)	% Data (6)	σ_{rms}[a] (μJy) (7)	$\Delta T_{rms}/T_{CBR}$[a] ($\times 10^{-5}$) (8)
10″	1024	2″	17.0	None	100.0	3.43	19.1
18	1024	4	34.1	355	43.3	4.37	7.5
30	512	8	34.1	178	20.2	6.20	3.8
60	512	16	68.2	78	6.0	10.38	1.6
80	512	16	68.2	43	1.5	16.60	1.5

[a] All values in column are for Lynx field. Multiply by 1.6 to obtain Cepheus field values.

The images calculated in this manner have an approximate full width at half-maximum resolution of about 10″, and an rms noise of 3.4 and 5.5 μJy per beam for the Lynx and Cepheus fields, respectively. Lower resolution images were also made by weighting down the longer spacings, using a Gaussian weighting function, or taper. The resulting noise levels are given in Table 1. Images in the Stokes parameters Q, U, and V were also produced. Because the Lynx field observations are more sensitive than those of the Cepheus field, the discussions in §§ 3, 4, and 5 will concentrate on the Lynx data. However, all analysis, reductions, and modeling were done in a similar manner on the Cepheus field, with the results given in § 5 as well.

A summary of the imaging parameters is given in Table 1. The image areas were made much larger than the field of view needed, in order to avoid some aliasing near its edge and to measure the image fluctuations as a function of distance to the field center. The Gaussian data taper given in column (5) is the distance at which the data were weighted by 50% of nominal in order to obtain the lower resolution images. The effective percentage of the data used and the rms noise for each resolution are given in columns (6) and (7). The rms noise values remaining after weighting were measured from the difference image (as described in § 4.2). The correspondence to rms brightness temperature is shown in the last column (see eq. [7] for conversion).

The range of usable resolutions follows naturally from the characteristics of the VLA. The highest resolution of 10″ comes from using *all* the visibility data. Somewhat higher resolutions can be obtained by weighting down the shorter spacings, but the noise level will increase markedly. The resolution of 80″, for which only visibility data less than projected 36 m spacing is given more than half-weight, is about the lowest resolution image that can be obtained from these data. There are no visibility data with spacing less than 25 m, since the projected separation of two antennas cannot be less than their diameter of 25 m.

Even full synthesis VLA images still contain sidelobes which are noticeable around strong sources. These artifacts were removed using the standard CLEAN algorithm, as described by Högbom (1974) and Schwarz (1978). In the deconvolution, we cleaned to a level of 1.5 times the image rms noise. This cleaning depth was required for the 10″ resolution image. We used a loop gain of 0.1 and approximately 20,000 iterations. Because the field contains a myriad of faint sources, such deep cleaning was necessary to remove their accumulated sidelobes and to determine accurate parameters for the detected sources.

The cleaned total-intensity contour images are shown for the Lynx and Cepheus fields in Figures 1 and 2 of Windhorst et al. (1993). Although the two fields were carefully selected to be free of sources greater than 1 mJy, about 20–30 fainter sources are clearly visible in each image. The brightest sources have flux densities of several hundred microjanskys, and any object with a peak flux density greater than about 4.5 times the rms noise is likely to be a radio source. The cataloging of the sources and an analysis of their properties in the two fields are discussed by Windhorst et al. (1993). The images contain an adequate number of microjansky sources to extend the count of sources several orders of magnitude lower than in previous surveys at 8 or 10 GHz (e.g., Aizu, Inoue, & Tabara 1987). Here our task is to remove their contribution to the fluctuations in the images.

3.2. *Removal of the Bright Source Contribution*

The "bright" sources were cataloged by Windhorst et al (1993). They were defined as sources with peak flux density in the 10″ cleaned image exceeding 4.5 σ, corresponding to 14.5 and 22.9 μJy, respectively, for the Lynx and Cepheus fields. There were 22 such sources in Lynx and 11 in Cepheus. Not all of the sources visible in the images are in the complete sample, because some of them are far from the field center where the primary-beam correction is too poorly known (see Windhorst et al. 1993). Three-quarters of the sources were smaller in angular size than 10″, and none was larger than 30″. Hence, there is little doubt that these faint features are discrete radio sources and not large-scale emission fluctuations in the sky. Optical identification on deep CCD frames is in progress and will be published in a subsequent paper in this series.

Although the 10″ resolution image is most sensitive for detecting point sources (as Table 1 shows), the lower resolution images are more sensitive to larger scale brightness temperature variations, which are proportional to the rms flux density times the resolution area. However, foreground discrete radio sources are blended in the lower resolution images and, hence, produce sky emission fluctuations which cannot be distinguished from CBR fluctuations (Franceschini et al. 1989). Since the discrete sources detected in the fields are generally less extended than 5″, we can use the high-sensitivity 10″ resolution image to determine the flux density, position, and angular size of *each* detected radio source, and remove its contribution from the visibility data. In this way, sources which would be below the detection limit at lower resolutions can be removed, and the image fluctuations caused by sources are significantly reduced in the lower resolution images.

"Strong" sources were removed in the following manner. From the source catalog (Windhorst et al. 1993), we selected the sources in each field above the 4.5 σ completeness limits listed above. We determined the total emission from each source by cleaning a 10″ × 10″ box around each source in the

10″ resolution image down to the 2 σ (7 μJy) level. The visibility function associated with these cleaned components was then calculated and subtracted from the original visibility data, to obtain the *residual* visibility data. Images constructed from the latter data are thus free of bright sources *and* their sidelobes for *all* resolution. In each of the 10″ × 10″ boxes surrounding the original bright sources, the image response has now been truncated to about the 2 σ level; this remaining intensity consists of both residual noise and residual source. The effects of this subtraction method are discussed in the next section.

4. VARIANCE ANALYSIS

4.1. *Sum and Difference Images*

As in Fomalont et al. (1988), we separated the residual visibility data set (with strong sources subtracted) for each field into two roughly equal independent parts.[4] Each half–data set was then imaged, *but not cleaned*, with the parameters and resolutions in Table 1.

The *sum* image is the average of the two (half–data set) images and represents the most sensitive image of the sky. The *difference* image was calculated by taking one-half of the difference between the two (half–data set) images and represents the noise characteristics of the image. Figures 1 and 2 (Plate 1) show the sum image on the left and the difference image on the right, at 10″ and 60″ resolution, respectively.

The difference image responses are dominated by receiver noise which produces a uniform variance level across the entire image. Very little sky emission or sidelobes should appear on the difference image. Although the receiver noise has a nearly perfect Gaussian distribution, convolution with the dirty beam pattern produces a mottled appearance, especially in the 60″ resolution image. Serious calibration errors or interference signals generally produce waves or spokes or circular features, preferentially near the image center. None are apparent in the difference images. A more detailed analysis of the statistical properties of the image is given in the next section.

The sum images on the left in Figures 1 and 2 appear similar to the difference images. Since all sources brighter than 14.5 μJy peak flux density have been removed, there are no bright intensity peaks within the image; however, the 10″ sum image does contain additional features, somewhat concentrated, near the center. These features do not appear particularly "pointlike" but may be the blends of weak sources in the sky. Similarly, the 60″ resolution sum image also has somewhat more "noise" near the center than that in the corresponding difference image.

The analysis of the properties of this additional noise and its interpretation in terms of instrumental effects, weak radio sources, and CBR fluctuations in the sky are described in the remainder of § 4 and in § 5.

4.2. *Analysis with Dirty Images*

A basic assumption in the following analysis is that the difference image is an excellent *control* sample which has the same statistical properties of all the *non-sky* noise components in the sum image. This assumption is valid if the following two conditions hold: (1) the response of all sky emission (including sidelobes) is identically the same on the images made from the two independent data sets, and (2) any additional image fluctuations from noise or calibration errors between the two half–data sets are *independent*.

The first assumption holds if the observing parameters for the VLA data in each half are the same. Most critical is that the *u-v* coverage should be nearly identical, so that the sidelobes of the sources are the same from each data set. This is the reason why we used alternating days, each with a similar *u-v* coverage, for separating the two half–data sets. The difference image, then, contains no sky emission, whether produced by source or by the sidelobes.

The second assumption—independent errors for each data set—is more difficult to assess. For errors which are correlated over periods of a day or less (receiver noise, short-term phase errors induced by the troposphere, interference, and many other calibration errors), separating the data by *alternating* days should produce similar stochastic fluctuations in *both* the sum and the difference image. On the other hand, errors which persist over the *entire* observation period of 15 days, or those that have a repeatable diurnal behavior, can produce similar artifacts in the image from each data half (e.g., any gain or phase errors which are a function of source elevation, or errors in the assumed global properties of the array). Such errors could produce no artifacts in the difference image if completely correlated between the two data sets, but would appear entirely in the sum image. Partial correlation would increase the fluctuations in the sum image, but less so than for the difference image. The frequent calibration of the VLA data using a nearby radio source calibrator should decrease these long-term systematic errors to low levels.

There is a crucial difference in the analysis of this experiment, compared with previous VLA experiments, to determine CBR fluctuations (Fomalont et al. 1984, 1988; Martin & Partridge 1988). The statistical analysis which follows here will be made on *dirty* images—that is, from images made *directly* from the visibility data with a Fourier transform with *no* subsequent cleaning or use of other image reconstruction techniques. We thus made no attempt to remove sidelobes of the myriad of weak sources in the field of view. While CLEANing an image clearly improves the quality of a discrete source and also decreases the general noise level, this process also modifies the statistical properties of the noise in an image. The aim of the cleaning algorithm is to replace a source (or noise spike) and its known sidelobe structure with a clean sidelobe-free source at the same resolution. Simulations by us and by others, however, have shown that the CLEAN algorithm is a nonlinear operation when approaching the noise level, especially when the source and the noise variance are of a comparable level. The CLEAN algorithm affects the noise statistics, and may even interchange variance noise between sources and a random Gaussian noise field. Furthermore, the modification of the statistics in a difference image, which contains nearly random Gaussian noise, is not identical to that in a sum image, which contains many faint sources in addition to noise. Finally, the CLEAN algorithm becomes more nonlinear at lower resolutions, where the sidelobe levels of the sources are comparatively larger.

As we have already noted in § 3.2, however, we did clean the 10″ resolution image in order to determine accurate parameters for the strong sources. The modification of the noise properties at low levels was of little concern in measuring the properties on the strong sources. The rms noise for the clean

[4] For the Lynx field we combined days 1, 3, 5, and 8 for one set, and days 2, 4, and 7 for the other set; it snowed on day 6. In order to keep their visibility coverage nearly the same—so that the sidelobes of the synthesized beam from both data halves are identical—we did *not* split any of the days between the two sets. The slight difference in the integration time between the two halves adds a few percent to the rms noise in the combined images.

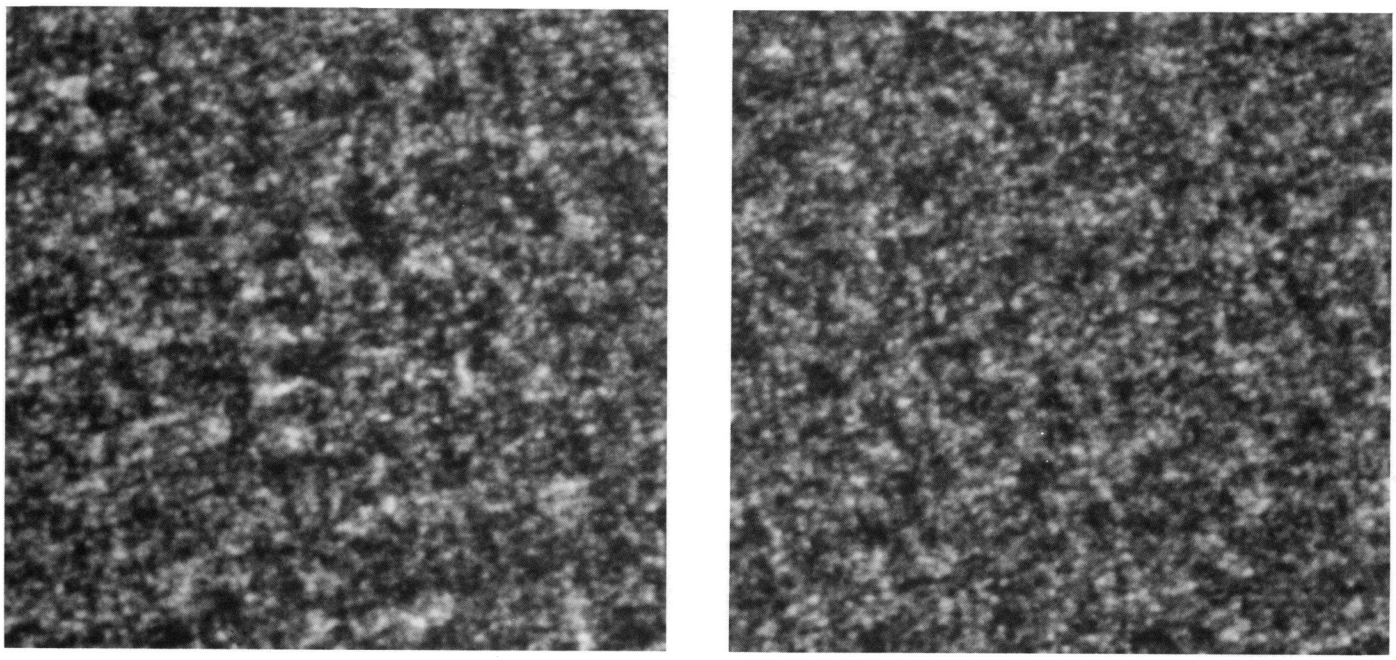

FIG. 1.—VLA 8.44 GHz residual images of the Lynx field with 10″ resolution. *Left*: sum image; *right*: difference image. The gray-scale display is -15 μJy (*black*) to $+15$ (*white*). The image covers an area of 8.′5 × 8.′5, but the full width at half-power diameter of the sky sensitivity is 5′. The noise variance of 11.8 μJy^2 is uniform over the difference image. The noise variance of the sum image is 15.8 μJy^2 near the center and 12.3 μJy^2 at the edge.

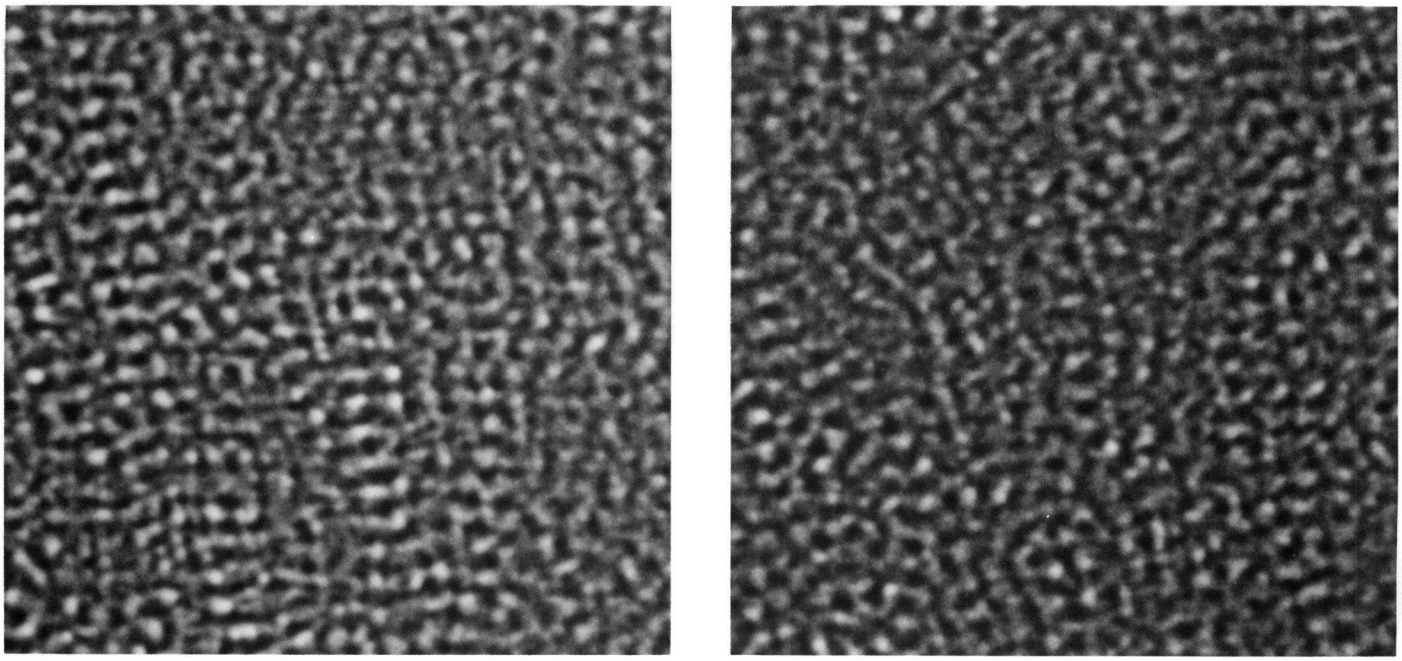

FIG. 2.—VLA 8.44 GHz residual images of the Lynx field with 60″ resolution. *Left*: sum image; *right*: difference image. The gray-scale display is -45 μJy (*black*) to $+45$ (*white*). The image covers an area of 34′ × 34′, but the full width at half-power diameter of the sky sensitivity is 5′. The noise variance of 108 μJy^2 is uniform over the difference image. The noise variance of the sum image is 197 μJy^2 near the center and 113 μJy^2 at the edge.

image of the Lynx field was 3.22 μJy (Windhorst et al. 1993), and the detection limit for bright sources was taken to be 4.5 times this rms, or 14.5 μJy. In contrast, the rms noise level in the dirty image after removal of the bright sources was 3.43 μJy (Table 1). The somewhat increased rms noise could be produced by CBR fluctuation in the sky; however, in § 5.2 we will show that this excess is consistent with that expected from the sidelobes of the myriad of faint sources and the noise peaks in the image. The theoretical noise level, based on the observing time, bandwidth, and receiver sensitivities is 3.14 ± 0.05 μJy. The increased rms in the clean and dirty images is produced by calibration errors which are discussed in § 5.2.

4.3. *Expected Angular Dependence of Image Variances*

The sum and difference images are dominated by quasi-random fluctuations, as seen in Figures 1 and 2. Hence, the relatively straightforward determination of the dependence of the variance of intensity fluctuations in the *sum* image, σ_s^2, and the *difference* image, σ_d^2, as a function of distance θ from the field center, adequately describes the information contained in these images. We will call these statistical measures the *image variance*, and they will generally be a function of distance from the field center.

The expected components of the image variance from these observations are

$$\sigma_d^2(\theta) = \sigma_n^2 + \sigma_u^2(\theta) , \quad \sigma_s^2(\theta) = \sigma_d^2(\theta) + \sigma_e^2(\theta) . \tag{1}$$

where σ_n^2 is the image variance expected from receiver noise alone, σ_u^2 is the contribution from uncorrelated calibration errors, and σ_e^2 is the *excess* variance associated with the sum image. For the ideal experiment whose synthesized beam has no sidelobes and has perfect calibration, we expect

$$\sigma_e^2(\theta) = P^2(\theta)\sigma_{\rm sky}^2 , \tag{2}$$

where $P(\theta)$ is the VLA primary-beam response, or sensitivity, as a function of distance θ from the field center, and $\sigma_{\rm sky}^2$ is the *total* sky emission variance at the resolution of the observations. Thus, any residual excess variations should be confined to the central part of the image where the primary-beam response is significant.

Because we analyzed dirty images, however, some of the power of a source is scattered well outside the formal sensitivity area of the image (especially for the lower resolution images). This broadens the angular scale of the excess variance, compared with that expected from the primary-beam sensitivity alone. The use of clean images minimizes this broadening but also alters the linear relationship between the variances caused by sky emission, receiver noise, and various instrumental errors in unknown ways.

The effect of nonperfect calibrations or other errors was discussed in § 4.2. If these errors are uncorrelated between the two half-data sets, both the difference and the sum images will contain the same contribution, but the excess variance will not be affected. If part of the errors are correlated, then there will be an additional component of the excess variance, $\sigma_c(\theta)$, which is present in the sum image but not in the difference image. In this case we expect that the following excess variance is

$$\sigma_e^2(\theta) = Q^2(\theta)\sigma_{\rm sky}^2 + \sigma_c^2(\theta) , \tag{3}$$

where $Q^2(\theta)$ is the effective sensitivity of the dirty image to the sky variance. If the synthesized beam had no sidelobes, $Q^2(\theta) = P^2(\theta)$. Sidelobes, however, increase the width of Q by scattering power from sources in the sky over a large part of the dirty image.

4.4. *Measured Angular Dependence of the Image Variance*

The variances from the residual images for the Lynx field at 10″ and 18″ resolutions for both the sum and the difference image are shown in Table 2. They were calculated in concentric rings with radial thickness of 100″ to ascertain the variance as a function of distance from the field center. The second column gives the area-averaged value of $P^2(\theta)$ for each ring. The two inner rings cover most of the primary beam, and the remaining rings have less than 3% sky sensitivity (Oort & Windhorst 1985). The first sidelobe of the primary beam is at a distance of 450″ from the field center, with a peak sensitivity of 2.7%. The number of independent beams, NB, in each ring at 10″ resolution is given in column (3). The average variances in units of μJy^2 for the sum image (σ_s^2) and the difference image (σ_d^2) are given in the next two columns. Since the variance in the difference image is nearly uniform over the entire image, we list the average variance, $\bar{\sigma}_d^2$, and its rms error, $\Delta\bar{\sigma}_d^2$, on the bottom line of the table.

The excess variance ($\sigma_e^2 = \sigma_s^2 - \bar{\sigma}_d^2$) and its estimated error are given in column (6). The error in σ_e^2 is calculated as $(\sigma_s^2(\mathrm{NB})^{-1/2} + \Delta\bar{\sigma}_d^2)$, where NB is the independent number of

TABLE 2

VARIANCE OF LYNX FIELD AT 10″ AND 18″ RESOLUTION

Ring Radii (arcsec) (1)	$P^2(\theta)$ (2)	Number of Beams (3)	10″ Variance (μJy^2) σ_s^2 (4)	σ_d^2 (5)	σ_e^2 (6)	18″ Variance (μJy^2) σ_s^2 (7)	σ_d^2 (8)	σ_e^2 (9)
0–100	0.78	314	15.83	11.49	4.05 ± 0.90	30.55	16.34	11.48 ± 3.11
100–200	0.27	942	15.19	12.14	3.41 ± 0.50	31.76	19.95	12.69 ± 1.87
200–300	0.03	1570	13.36	11.96	1.58 ± 0.35	24.57	19.12	5.50 ± 1.13
300–400	0.01	2199	12.46	11.42	0.68 ± 0.28	21.27	18.98	2.20 ± 0.84
400–500	0.02	2827	12.52	11.59	0.74 ± 0.25	22.57	18.08	3.50 ± 0.78
500–600	0.01	3455	12.51	11.79	0.73 ± 0.23	21.43	19.84	2.36 ± 0.68
600–700	0.00	4084	12.80	11.89	1.02 ± 0.22	22.85	19.30	3.78 ± 0.67
700–800	0.00	4712	11.92	11.79	0.14 ± 0.19	20.30	18.82	1.23 ± 0.56
800–900	0.00	5340	12.02	12.04	0.24 ± 0.19	19.80	19.46	0.73 ± 0.52
900–1000	0.00	5969	12.35	11.60	0.57 ± 0.18	20.86	18.16	1.79 ± 0.52
0–1000[a]	...	...	...	11.78 ± 0.08	...	...	19.07 ± 0.22	...

[a] Average difference variance and its rms error.

TABLE 3

VARIANCE OF LYNX FIELD AT 30″, 60″ AND 80″ RESOLUTION

RING RADII (arcsec) (1)	$P^2(\theta)$ (2)	NUMBER OF BEAMS (3)	30″ VARIANCE (μJy^2) σ_s^2 (4)	σ_d^2 (5)	σ_e^2 (6)	60″ VARIANCE (μJy^2) σ_s^2 (7)	σ_d^2 (8)	σ_e^2 (9)	80″ VARIANCE (μJy^2) σ_s^2 (10)	σ_d^2 (11)	σ_e^2 (12)
0–200	0.40	139	73.4	33.7	34.9 ± 6.2	197.4	85.6	89.6 ± 33.8	344.0	223.0	68.6 ± 80.7
200–400	0.01	418	48.6	38.2	10.2 ± 2.3	139.9	103.6	32.0 ± 13.0	363.7	270.6	88.2 ± 45.9
400–600	0.02	698	48.3	38.6	9.9 ± 1.9	146.2	109.2	38.4 ± 11.2	369.5	300.6	94.1 ± 37.9
600–800	0.00	977	46.2	37.7	7.8 ± 1.5	132.0	98.1	24.1 ± 8.5	328.3	251.0	52.7 ± 27.8
800–1000	0.00	1256	41.4	37.3	2.9 ± 1.2	116.1	106.5	8.2 ± 6.8	275.4	278.7	0.0 ± 21.5
1000–1200	0.00	1535	42.1	37.4	3.6 ± 1.2	117.2	100.4	9.4 ± 6.3	294.6	249.7	19.2 ± 21.0
1200–1400	0.00	1815	40.0	37.4	1.5 ± 1.0	115.3	103.2	7.5 ± 5.8	301.1	260.7	25.7 ± 19.7
1400–1600	0.00	2094	40.3	39.1	1.9 ± 1.0	107.9	116.0	0.1 ± 5.1	254.0	297.7	−21.5 ± 15.9
1600–1800	0.00	2373	41.6	40.6	3.2 ± 1.0	114.5	115.8	6.6 ± 5.1	273.1	293.3	−2.3 ± 16.1
1800–2000	0.00	2652	40.9	38.6	2.4 ± 0.9	112.4	109.4	4.5 ± 4.8	273.2	278.6	−2.2 ± 15.4
0–2000	...	...	...	38.5 ± 0.5	...	...	107.8 ± 2.3	...	...	275.4 ± 6.2	...

beams within the ring. The reason for using the average difference variance $\bar{\sigma}_d^2$ rather than σ_d^2 from each ring will be discussed in § 4.5.

The results for the 18″ resolution image are also given in Table 2 in columns (7)–(9) in the same format as that for the 10″ image. The number of independent beams at 18″ resolution is 0.31 of that at 10″ resolution. Table 3 shows the variances for the Lynx field for 30″, 60″, and 80″ resolution in the same format as that in Table 2. The number of independent beams at 30″ resolution should be scaled accordingly for the lower resolutions. Because of the lower resolution, a ring thickness radius of 200″ was used in order to obtain a reasonable number of independent beam samples in the inner ring.

4.5. *Effect of Strong Source Subtraction*

Tables 2 and 3 show that the mean value of the fluctuations in the *difference* images at all resolutions is relatively constant over the entire field of view. This property is expected from receiver-noise–dominated statistics.[5] The average value of 11.78 μJy^2 for the 10″ resolution is somewhat larger than that expected from receiver noise alone, $\sigma_n^2 = 9.96$ μJy^2. In § 5.2 we show that this increase of 1.8 μJy^2 is consistent with that expected from typical calibration errors.

There is, however, a small but statistically significant decrease in the variance for the inner ring at *all* resolutions. The effect is about 10% and is smaller than that associated with the statistical errors. However, it is a systematic error, and we must understand its origin in order to have more confidence in the results of this experiment. This decrease is produced by the subtraction procedure which removed the visibility contribution of the bright, cataloged sources in order to obtain the residual visibility data sets (as described in § 3.2). Within the 22 source boxes of the Lynx field, each of angular size 10″ × 10″, the residual noise is also reduced, since the source model includes noise as well as real sky emission. In the 10″ resolution image where the cleaning was done, approximately 10% of the area within the inner 200″ ring lies within the 22 cleaning boxes. Thus, we expect that the variance of the difference image in this ring would be about 10% less than the variance of other rings which contain no sources. For lower resolution images, the decrease is more than 10% because the removal of noise peaks from the cleaning boxes also removed their corresponding sidelobes outside the boxes. To minimize this effect, we have thus used the mean variance $\bar{\sigma}_d$ over the entire difference image, rather than the individual ring rms values, as the best estimate of the noise variance for any ring.

The decrease of noise in the inner ring of the *sum* image is similar, in a statistical sense, to the decrease in the difference image. However, the residual bright source emission is also present within the 22 source boxes in the sum image. To determine the change in the variance near the center of the sum image, we have simulated the cleaning of a source in the presence of noise down to the 2 σ level. We find that the decrease in the noise variance in the boxes is about equal to the residual source variance, although it does depend on the angular size of the source to some extent. Therefore, the measured variances in Tables 2 and 3 of σ_s^2 within the inner ring are relatively unbiased estimates of the *true* variance in these rings which would have been obtained had the sources been completely removed and with the full noise contribution.

4.6. *Excess Variance*

Tables 2 and 3 (see also Table 4, col. [2]) show that there is significant excess variance near the center of the field for all resolutions. The excess is about 3.6 ± 0.4 μJy^2 at 10″ resolution and increases to nearly 100 μJy^2 at lower resolutions.[6] This apparent variance increase with lower resolution occurs because the variance units are in square microjanskys per pixel. The increase is, in fact, consistent with a population of point sources in the field. At 10″ resolution, for example, the radio image is relatively empty and most pixels are free of brighter sources and therefore near zero intensity. At 30″ resolution weak sources are spread in the image over a larger area (but with the same peak intensity), and more pixels have, thus, significant nonzero value. Hence the excess variance at 30″ resolution from point sources should be about 9 times that at 10″ resolution. This ratio is observed. At progressively lower resolutions when the sources and sidelobes begin to blend, the excess variance does not increase as fast as the square of the resolution, which is observed between 30″ and 80″ resolution.

[5] Only the inner quarters of the images have been used in the variance analysis. Effects near the edge of an image which increase the noise contribution slightly are insignificant in the region analyzed.

[6] The excess variance in the original images in which the bright sources were not removed are about a factor of 6 larger than those in Tables 2 and 3. The excesses in the inner rings are 24, 67, 150, 400, and 700 μJy^2 at 10″, 18″, 30″, 60″, and 80″ resolutions, respectively.

The excess variance does not decrease with angular distance from the field center as quickly as the primary-beam sensitivity, $P^2(\theta)$, and also extends well beyond the limits of the primary-beam sensitivity. This slow drop-off in angle is particularly striking for the lower resolution images, and is clearly produced by scattered flux from the accumulated sidelobes of the faint sources in these dirty images. Because these sidelobes are nearly the same for both data sets, they cancel to first order on the difference image but not on the sum image.

5. EFFECT OF WEAK SOURCES

Based on the properties of the sources stronger than 14.5 μJy (Windhorst et al. 1993), we can estimate the contribution and range of contribution of weaker sources.

5.1. *Simulation of Variance Produced by Weak Sources*

In order to determine the effect of weak sources on the image variance, we simulated our actual VLA observations as carefully as possible. The modeling can be summarized as follows:

1. We used the following density of sources in the sky:

$$n(S) = (19 \pm 3)S^{-1.3\pm0.2}, \quad (4)$$

where n is the average number of sources per square arcminute with an 8.44 GHz flux density greater than $S(\mu\text{Jy})$. This is the value obtained by Windhorst et al. (1993) for the flux density range between 14.5 and 1000 μJy. Since the slope of the counts between 15 and 1000 μJy is nearly constant at 8.44 GHz and at 4.9 GHz (Fomalont et al. 1991), extrapolation of the counts with the same slope to lower flux densities is reasonable. The effect of departures of the count from that in equation (4) is discussed in § 5.2 and in Windhorst et al. (1993). As we shall see in the modeling, the flux density of a typical source which contributes to the observed excess variance is about 7 μJy, so the count extrapolation extends only a factor of 2 from the lower limit of the discrete source catalog.

2. We adopted the angular size distribution found by Windhorst et al. (1993). The median angular size of the sources is 3.″5, while about one-quarter of them are larger than 10″. This angular size is similar to that found at 4.9 GHz for microjansky sources (Fomalont et al. 1991) and is somewhat larger than the angular size at mJy levels (Windhorst et al. 1990). The instrumental bandwidth smearing ($\approx$4″ at the edge of the primary beam) was also included in this simulation. With the maximum resolution of 10″, however, the effect of finite source size is relatively unimportant.

3. We randomly populated an area of radius 7′ with sources with the above distributions. This area extends out to the first sidelobe of the primary beam, so effects of confusing sources outside the main field of view are also included. All sources with a peak flux density greater than 14.5 μJy (22.9 μJy for the Cepheus field) at 10″ resolution were subtracted from the simulated image, just as they were from the original image. We found that sources with flux density less than 0.5 μJy contributed insignificantly to the image variance, so these sources were not included in the simulated sky population. Hence, even if the slope of the integral μJy counts remains at 1.3, the contribution to the sky variance is small, although the contribution to the total sky brightness is not (Windhorst et al. 1993).

4. We calculated the visibility function for this simulated sky at the identical (u, v) points sampled by the observations.

5. We imaged the simulated data with the same parameters as those used for the real data.

6. We determined the excess variance of the simulated images in each ring for the five resolutions of Tables 2 and 3 in the same manner as for the real data.

7. Steps 1–6 were processed with five different sets of randomly generated sources in the sky. From the set of simulated images we determined the mean variance expected from *weak* foreground sources, σ_w^2.

The estimated error of the weak source variance is composed of two parts. The first part is the standard deviation of a typical model about the average determined from the set of five trials. This error should be an accurate measure of the typical field-to-field variation expected in the distribution of weak radio sources, and for the 10″ resolution image it is equal to about 10% of the mean variance. At lower resolution this percentage increases, since the number of sources in the relevant flux density range decreases and more statistical variation is expected. If the redshift distribution of weak radio sources shows significant superclustering (e.g., Windhorst et al. 1990), the field-to-field differences could be twice as large.

The second part of the estimated model error is associated with the uncertainty in the extrapolation of the count below the 14.5 μJy cutoff of the discrete source catalog. For the 10″ resolution image about 80% of the variance is produced by sources in the range 4–14 μJy. For the 18″ range the corresponding range is 5–25 μJy. For the 30″ image the range is 7–30 μJy, and for the 60″ image the range is 11–45 μJy. For the 80″ image the lower end of the range is 15 μJy, so no extrapolation is needed for this resolution. We used the 8.44 GHz counts from Windhorst et al. (1993)—together with the 10 GHz count of stronger sources (Aizu et al. 1987), and the deep 4.9 GHz counts (Fomalont et al. 1991), suitably transformed to 8.44 GHz—to estimate the uncertainty in the extrapolation of the counts to levels less than 14.5 μJy. Above 30 μJy the uncertainty in the average surface density of sources is about 7%. counts from Windhorst et al. (1993)—together with the 10 GHz count of stronger sources (Aizu et al. 1987), and the deep 4.9 GHz counts (Fomalont et al. 1991), suitably transformed to 8.44 GHz—to estimate the uncertainty in the extrapolation of the counts to levels less than 14.5 μJy. Above 30 μJy the uncertainty in the average surface density of sources is about 7%. The uncertainty increases for weaker sources, since the slope of the count may also be in error. At 14.5 μJy the error is 10%, and it increases to 20% at 5 μJy. We estimate, then, that the count uncertainties at resolutions 10″, 18″, 30″, 60″, and 80″ are 15%, 13%, 10%, 7%, and 7%, respectively. The estimated error in the model variance for the count uncertainty can then be calculated at each resolution.

5.2. *Comparison of Observed and Model Variance: Calibration Errors*

The comparisons of the observed *excess* variance σ_e^2 with the estimated *weak* source variance σ_w^2 are shown in Table 4. We have averaged the excess variances over several rings in Tables 2 and 3 and give the results for (1) the 0″–200″ ring, which contains most of the primary-beam area; (2) the 200″–1000″ ring, which is at the edge of the primary-beam region; and (3) the 1000″–2000″ ring, well outside the primary-beam area. The estimated error was determined from the errors in the individual rings and from the scatter of values among the rings.

The difference between the measured excess and weak-source variance in the image is called the *residual* variance, σ_r^2, and is also shown in Table 4 for the three rings. The error of

TABLE 4

EXCESS, WEAK-SOURCE, AND RESIDUAL VARIANCES

	Ring Radii								
	0″–200″			200″–1000″			1000″–2000″		
Resolution (1)	σ_e^2 (2)	σ_w^2 (3)	σ_r^2 (4)	σ_e^2 (5)	σ_w^2 (6)	σ_r^2 (7)	σ_e^2 (8)	σ_w^2 (9)	σ_r^2 (10)
10″	3.62 ± 0.43	2.73 ± 0.80	0.89 ± 0.91	0.73 ± 0.12	0.33 ± 0.20	0.40 ± 0.23	...	...	...
18	12.36 ± 1.71	9.61 ± 2.92	2.75 ± 3.38	2.44 ± 0.42	0.84 ± 0.31	1.80 ± 0.52	...	...	...
30	34.9 ± 6.2	28.0 ± 7.1	6.9 ± 9.4	6.6 ± 1.6	1.3 ± 1.2	5.3 ± 2.0	2.3 ± 0.8	1.0 ± 0.5	1.3 ± 1.0
60	89.6 ± 33.8	82.4 ± 28.6	7.2 ± 44.3	18.3 ± 6.2	2.3 ± 3.0	16.0 ± 6.9	5.3 ± 4.1	1.3 ± 4.0	4.0 ± 6.3
80	69 ± 81	119 ± 116	−50 ± 144	42 ± 22	11 ± 25	31 ± 33	8.2 ± 6.1	5.2 ± 6.0	3.0 ± 8.6

the residual variance is the rms sum of the excess and model variances. At most resolutions the error associated with the modeling of weak sources is larger than the statistical uncertainty associated with the measured excess variance.

Following the discussion in § 4.3 concerning equation (3), we expect the following residual variance:

$$\sigma_r^2(\theta) = Q^2(\theta)\sigma_{r\mathrm{sky}}^2 + \sigma_c^2 , \quad (5)$$

where $\sigma_{r\mathrm{sky}}^2 = \sigma_{\mathrm{sky}}^2 - \sigma_w^2$ is the *residual sky* variance after removal of the weak sources. Two obvious conclusions from Table 4 are that the residual variance in the inner ring tends to be positive, but consistent with zero within the statistical uncertainty, and that the residual variances in the outer two rings are also positive. This residual can arise in several ways: (1) from CBR fluctuations at the level of about 1 σ; (2) from a surface density of weak sources in the Lynx field somewhat larger (again by about 1 σ) than that assumed in the modeling described in § 5.1; or (3) from the correlated error component σ_c^2 between the two half-data sets.

An estimate of the effect of *typical* calibration errors for the VLA system is consistent with the variances observed in this experiment: the 0.9 μJy^2 residual excess in the sum image is produced by correlated calibration errors; and the 1.8 μJy^2 excess variance of the difference image over that expected from the system noise (see § 4.5) is produced by uncorrelated calibration errors. The typical dynamic range for an image made at the VLA at a frequency of 8 GHz in the D-configuration is about 100:1. This means that the image contains error signals which are about 1% of the peak flux density of each source within the field, including the bright sources which were subtracted to obtain the residual images. The individual contributions will add randomly and are centered around zero intensity. The rms sum of the flux density of the weak sources in the modeling is about 70 μJy, and the rms sum of the strong sources which were subtracted is 150 μJy. Thus, a typical variance produced by errors in the calibration is about 2.2 μJy^2. The separation of this variance into the correlated and uncorrelated components depends on the nature of the calibration errors and is unknown. The two contributions are probably comparable. Thus, the measured values of σ_u^2 and σ_c^2 are consistent with expected calibration errors.

5.3. *Conversion of Image Variance to Sky Variance*

Table 5 shows the conversion of the measured residual variance in the *image* to the *sky* for the Lynx field. Column (1) gives the approximate resolution of the image, and column (2) lists the residual variance and the error estimate from the 0″–200″ ring data in Table 4. This variance is the estimate of the fluctuation component in the image after removal of strong and weak sources, with their sidelobes, and any uncorrelated calibration errors. As discussed above, there is a small positive residual variance at most resolutions, which may be produced by (1) CBR fluctuations in the sky, (2) a larger than expected contribution from weak sources, or (3) correlated calibration errors between the two data halves. For the 80″ resolution image we have listed two entries: the second is the excess variance σ_e^2 without the variance of the weak sources removed. Because of the weak-source modeling error, the 95% confidence limits derived from this measurement, which has smaller errors, are less than for the variance corrected for the weak sources, which has larger errors.

The conversion of the image variance in square microjanskys to sky variance in square microjanskys depends on the sensitivity of the dirty image to the sky variance, $Q^2(\theta)$, given in equations (3) and (5). It is the ratio of the variance in the image produced from any sky variance, and Q depends on the primary-beam sensitivity of the VLA antennas, the sidelobe pattern in the dirty beam, and the nature of the fluctuations in the sky. Using the analysis method in the Appendix, we have calculated $Q^2(\theta)$ as a function of distance from the field center, using the known primary-beam sensitivity and the sidelobe pattern, for several fluctuation spectra in the sky. Near the field center $Q^2(\theta)$ is somewhat less than 1.0 (about 0.95), but its value decreases less rapidly with field-center distance than $P^2(\theta)$. For all reasonable fluctuation spectra of sky emission, the average image fluctuations in the central ring of radius 200″ is $\approx$40% of the sky fluctuations. This is the ratio that is also obtained from simply averaging the average primary beam response $P^2(\theta)$ over the central ring; hence the sidelobes of the sources do not substantially change the image-to-sky fluctuations near the beam center. We, thus, have multiplied the residual image variance in column (2) by 2.5 in order to obtain the residual sky variance, shown in column (3).

TABLE 5

LIMITS TO SKY VARIANCE IN LYNX FIELD

	Residual Variance σ_r^2		95% Confidence:
Resolution (1)	Image (μJy^2) (2)	Sky (μJy^2) (3)	Sky (μJy^2) (4)
10″	0.89 ± 0.91	2.22 ± 2.28	<5.98
18	2.8 ± 3.4	7.0 ± 8.5	<21.0
30	6.9 ± 9.4	17.2 ± 23.5	<56.0
60	7 ± 44	18 ± 110	<200
80	−40 ± 144	−100 ± 360	<594
80[a]	69 ± 81	172 ± 203	<507

[a] Weak sources included.

TABLE 6

LIMITS TO SKY VARIANCE IN CEPHEUS FIELD

RESOLUTION (1)	RESIDUAL VARIANCE σ_r^2: Image (μJy^2) (2)	RESIDUAL VARIANCE σ_r^2: Sky (μJy^2) (3)	95% CONFIDENCE: SKY (μJy^2) (4)
10″	1.6 ± 3.6	4.0 ± 9.0	<18.8
18	0.8 ± 13.3	2.0 ± 33.2	<56.8
30	−35 ± 31	−88 ± 78	<129
60	−116 ± 104	−290 ± 260	<429
80	−134 ± 266	−335 ± 665	<1097
80[a]	−12 ± 222	−30 ± 555	<915

[a] Weak sources included.

Column (4) gives the 95% confidence upper limit of the sky variance. If we assume that the error quoted in column (3) is the standard deviation of a Gaussian distribution of possible experimental outcomes—of which this one is a random sample—then the upper limit to the sky variance is equal to 1.65 times the quoted standard error, plus the mean variance. If the mean variance is less than zero, we have not added its contribution. We feel that the use of more sophisticated statistical tests to determine the limits are unwarranted.

All of the reductions, analysis, and modeling described for the Lynx field were also repeated for the Cepheus field. Because of the shorter integration time, limited u-v coverage, and inclement weather for Cepheus observations in 1988, the quality of the images is not as good as those for the Lynx field (see Windhorst et al. 1993). For the Cepheus field only sources brighter than 21.5 μJy were removed from the data, and the sky simulations were suitably adjusted.

Table 6 contains the results for the Cepheus field. Its format is identical to that of Table 5. Even with reduced sensitivity, this field also suggests the lack of fluctuations, and 95% confidence upper limits are given for the sky variance, which are about a factor of 1.6 larger than in the Lynx field, as expected from the ratio of the rms noise in the images from the two fields.

5.4. *Limits to CBR Fluctuations*

The combined results from the two fields on limits to the CBR fluctuations are given in Table 7. Column (1) lists the nominal resolution of the image (used throughout the paper as a convenient tag for the images), but the second column gives the precise resolution. Its calculation is described in connection with equation (7). The next column shows the average residual image variance for the combined Lynx and Cepheus fields. The variances were calculated from the weighted average of the Lynx and Cepheus variances, with a weight equal to the square of the inverse error. Conversion to sky variance and a 95% confidence limit was obtained in the same way as for Tables 5 and 6. The results are clearly dominated by the results from the Lynx image.

TABLE 7

LIMITS TO CBR FLUCTUATIONS (both fields)

RESOLUTION: Nominal (1)	RESOLUTION: Effective (2)	RESIDUAL VARIANCE σ_r^2: Image (μJy^2) (3)	RESIDUAL VARIANCE σ_r^2: Sky (μJy^2) (4)	95% CONFIDENCE LIMITS: Sky (μJy^2) (5)	95% CONFIDENCE LIMITS: $\Delta T_r/T_{CBR}$ ($\times 10^{-5}$) (6)
10″	13.″8	0.97 ± 0.87	2.43 ± 2.18	<6.03	<7.2
18	20.9	2.7 ± 3.4	6.8 ± 8.5	<20.8	<5.8
30	30.7	3.4 ± 9.0	8.5 ± 22.5	<45.6	<4.0
60	56.6	−11 ± 41	−28 ± 103	<170	<2.3
80	78.3	−61 ± 126	−153 ± 315	<520	<2.1
80[a]	78.3	60 ± 73	150 ± 183	<452	<1.9

[a] Weak sources included.

The conversion of flux density S at some resolution Ω to brightness temperature T at a frequency ν is given by

$$S(\mathrm{Jy}) = 3.07 \times 10^4 \Omega(\mathrm{sr}) \nu^2(\mathrm{GHz}) T(\mathrm{K}) . \quad (6)$$

This is the Rayleigh-Jeans approximation (e.g., Lang 1980, eq. [1-133]), which is valid at radio frequencies less than 15 GHz. Inserting more convenient units with $\nu = 8.44$ GHz, we obtain

$$\left(\frac{\Delta T(\mu\mathrm{K})}{2.735}\right)^2 = 5.56 \times 10^7 \frac{\sigma^2(\mu\mathrm{Jy}^2)}{\Omega^2(\mathrm{arcsecs}^2)} . \quad (7)$$

We determined the solid angle at each of the five resolutions in the following manner. First, we defined the beam region as the main response of the dirty beam out to the first zero. We then summed all of the pixel intensities within this region. The center of the dirty beam is defined as unity, so the sum of the pixel values times the area of each pixel is the solid angle of the beam. The effective resolution is given in column (2) of Table 7 in terms of the equivalent full width at half-power size of a Gaussian-shaped beam with the same solid angle measured for the dirty beam ($\Omega = 1.133\ \theta^2_{\mathrm{FWHP}}$). The nominal resolutions given in column (1) are a convenient tag for the individual images, but the effective beam size must be used to convert from flux density to kelvins.

Using equation (7) with the effective resolutions, we list in column (6) the upper limits for CBR fluctuations in the sky at the five image resolutions. We give the rms value rather than the variance. The limits are not tied to any specific model of fluctuation spectrum in the sky but represent the total variance in the sky inferred from the images.

The discussion of the robustness of these results is given in § 6.1. The interpretation of these limits in terms of specific two-point correlation functions of sky fluctuations is given in §§ 6.2 and 6.3.

Although we have *not* detected fluctuations, the formal results are impressive. At 60″ resolution we have measured sky fluctuations of $\Delta T/T_{\mathrm{CBR}} = (-2 \pm 17) \times 10^{-6}$; at 80″ resolution the measurement gives $(6 \pm 10) \times 10^{-6}$, where the contribution from weak sources has not been removed. This experimental sensitivity is consistent with the brightness temperature sensitivity of these observations, which were listed in Table 1.

5.5. *Limits to CBR Fluctuations of Polarized Radiation*

Images were made in the Stokes parameters V for circular polarization and Q, U for linear polarization. We also used the two half-data sets and analyzed the image variance in the same manner as for the total intensity I. The results from the Lynx and Cepheus fields were combined. Because extragalactic "foreground" sources emit radio waves which are usually less than 1% circularly polarized and ~3% linearly polarized, their contribution to the polarized sky background is not important and no discrete source contribution is expected.

Table 8 contains the limits for fluctuations in the circularly polarized component of the CBR. The limits are generally lower than that of the total intensity fluctuations at the higher

TABLE 8

LIMITS TO CBR FLUCTUATIONS: CIRCULARLY POLARIZED

Resolution		Residual Variance σ_r^2		95% Confidence Limits	
Nominal (1)	Effective (2)	Image (μJy^2) (3)	Sky (μJy^2) (4)	Sky (μJy^2) (5)	$\Delta T_r/T_{CBR}$ ($\times 10^{-5}$) (6)
10″	13.″8	0.47 ± 0.72	1.18 ± 1.80	<4.10	<5.9
18	20.9	1.5 ± 2.0	3.8 ± 4.8	<11.6	<4.3
30	30.7	4.1 ± 6.8	10.2 ± 17.0	<37.7	<3.6
60	56.6	−19 ± 38	−48 ± 95	<154	<2.2
80	78.3	78 ± 92	195 ± 230	<567	<2.2

resolutions where the foreground source contamination is a significant source of error. Limits to the linearly polarized component of the CBR fluctuations are given in Table 9. The polarized image, P, was calculated from the Q and U Stokes parameter images using $P = (Q^2 + U^2)^{1/2}$. The mean image variance and rms scatter about the mean were determined in the same rings from the Lynx and Cepheus fields independently, and then averaged in the same manner as the other polarizations. Column (3) lists the mean and rms image variance at the five resolutions. Since the linear polarization is the rms sum of the Q and U Stokes parameters, it is only defined for positive values. If the fluctuations are produced by receiver noise, the variance probability function has a Rayleigh distribution. If s is the standard deviation associated with a Rayleigh distribution,

$$R(x) = \frac{x}{s^2} \exp\left[-\frac{1}{2}\left(\frac{x}{s}\right)^2\right],$$

then the *mean* value is 1.25s, the rms scatter about the mean value is 0.81s. Thus, the *average* variance should be somewhat larger than the estimated rms, and there is a 5% chance that a randomly chosen value will exceed 2.45s, or 3.03 times the rms scatter. In Table 9 we have thus calculated the 95% confidence level as 3.03 times the rms of the residual variance in column (3). The mean value, which is expected to be about 1.55s, was thus *not* used in deriving the limits.

6. DISCUSSION OF THE DERIVED LIMITS

6.1. *Are the Limits Realistic?*

From long integrations with the VLA at 8.44 GHz on two small regions of the sky, we have determined limits to CBR fluctuations in the range of angular scales 10″–200″. These limits were obtained from the value and uncertainty of residual fluctuations in the dirty image (Table 7, col. [3]) which remain after (1) removal of strong "foreground" radio sources, (2) subtraction of the *estimated* statistical fluctuations from weak foreground sources below the detection limit of the discrete source catalog, and (3) subtraction of the *measured* statistical fluctuations from uncorrelated instrumental noise and errors. The estimated uncertainty of the measured residual image variance (which is generally larger than the residual itself) is dominated by two major contributions: the receiver noise from the telescope electronics and the uncertainty in estimating the density of weak discrete sources. Since these errors are independent and can be estimated with sound statistical arguments, the quoted error of the residual variance should be realistic and representative for the standard deviation in the normal distribution of possible values, from which this experiment has extracted *one* sample. The upper limit with 95% probability is equal to 1.65 times the standard deviation, plus the measured residual variance, if it is positive.

Several sources of systematic error are present and have been discussed. First, the surface density of weak sources was estimated, and their contribution to the observed variance was removed. A description of the procedure and an error estimate are given in § 5.1. A discussion of the extrapolation of the count below 14.5 μJy is given by Windhorst et al. (1993) and is consistent with the modeling used in this paper. Even with the *extreme* assumption that there are *no* weak sources in the image below the detection level, the entire excess variance at 10″ resolution of 3.62 ± 0.43 μJy^2 gives a limit (95% confidence) of less than 4.3 μJy^2. The residual variance, after a correction for weak sources of 0.89 ± 0.91 μJy^2, gives the upper limit of 2.4 μJy^2. Thus, complete disregard of the effects of weak sources increases the derived rms limits of CBR fluctuations by about 35% [$(4.3/2.4)^{1/2}$] at 10″ resolution. The increase at lower resolutions is even less.

The discussion in § 5.2 showed that the 1 σ level of 0.9 μJy^2 in the residual variance could be produced by long-term correlated errors between the two half-data sets. The short-term uncorrelated errors probably produced the 1.8 μJy^2 increase in the difference image variance from that expected from the receiver noise alone. However, these contributions cannot be quantitatively removed from the residual variance unless the properties of these errors can be independently measured. Other unsuspected errors that significantly impact the results of this experiment are unlikely because of the "triple difference" observational and reductions technique: (1) calibration of the radio fields with a nearby radio source, (2) comparison of the images from two independent halves of the experiments, and (3) comparison of the inner part with the outer part of the images. Such a difference technique removes error contributions which may not be understood but are temporally and spatially well behaved. Also, most of the image construction and analysis is linear (except strong source subtraction) in the sense that the image variance is the sum of the contributing effects in the instrument and in the sky.

A systematic error has, in fact, been produced by the method used to subtract out the strong sources, as discussed in § 4.4. The variance in the difference image is slightly depressed in the center of the field. We understand this effect, and have corrected it by using the *average* variance in the entire difference image as applicable to any region. The sum image is relatively unaffected by this subtraction method. However, complete disregard of this correction would not significantly change the derived limits.

TABLE 9

LIMITS TO CBR FLUCTUATIONS: LINEARLY POLARIZED

Resolution		Residual Variance σ_r^2		95% Confidence Limits	
Nominal (1)	Effective (2)	Image (μJy^2) (3)	Sky (μJy^2) (4)	Sky (μJy^2) (5)	$\Delta T_r/T_{CBR}$ ($\times 10^{-5}$) (6)
10″	13.″8	0.31 ± 0.74	0.78 ± 1.85	<5.61	<6.9
18	20.9	2.1 ± 2.0	5.2 ± 4.8	<14.5	<4.8
30	30.7	8.4 ± 4.1	21.0 ± 10.2	<30.9	<3.3
60	56.6	42 ± 31	105 ± 77	<233	<2.6
80	78.3	150 ± 72	375 ± 180	<545	<2.1

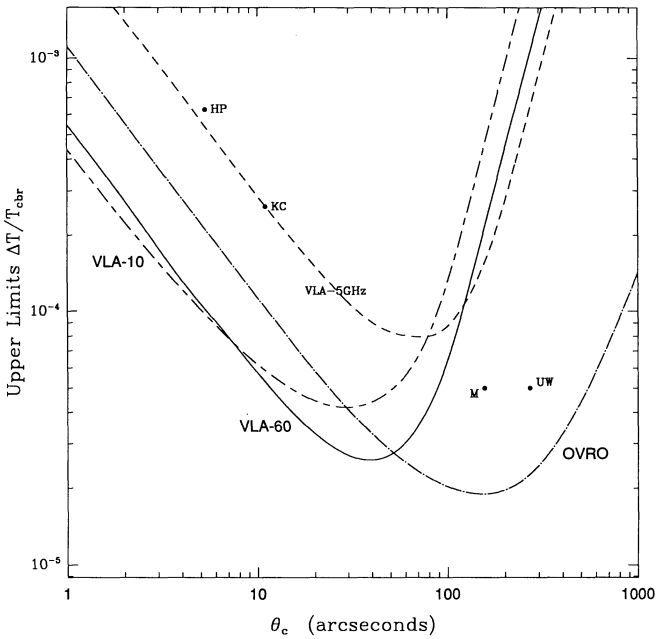

FIG. 3.—Limits to the observed Gaussian random fluctuations of the CBR between coherence angles 1″ and 1000″. The results from the 60″ and 10″ resolution images from this experiment are shown by the curves labeled VLA-60 and VLA-10. The previous VLA 5 GHz experiment with 60″ resolution, and the OVRO NCP experiment are also given. The results of four other experiments have been plotted at the angular scale of their most accurate result: UW = Uson & Wilkinson (1985); HP = Hogan & Partridge (1989); KC = Kreysa & Chini (1989); M = Myers et al. (1993).

6.2. *Comparison with Previous Measurements*

In Figure 3 we have plotted the 95% confidence limits from the VLA experiment for random Gaussian fluctuations in the sky over a range of coherence angle θ_c. We have followed the method outlined by Readhead et al. (1989), and the formulae are given in the Appendix. The most sensitive limits come from the 60″ resolution image.[7] With the measured upper limit of the image variance, $C_{obs}(0) = 67.6\ \mu Jy^2$, we used equation (A5) to determine C_0, the variance of the fluctuations defined in equation (A3). We have also plotted the results using the 10″ image with $C_{obs}(0) = 2.41\ \mu Jy^2$, and somewhat better limits are obtained at higher resolution.

The most sensitive limits—$\Delta T/T_{CBR} < 3.0 \times 10^{-5}$—occur within the range $22'' < \theta_c < 60''$. The minimum is 2.5×10^{-5} at $\theta_c = 40''$. The brightness temperature limit increases outside this range, but the 95% confidence limit of $\Delta T/T_{CBR} < 10 \times 10^{-5}$ is still obtained at $\theta_c = 5''$ and $\theta_c = 120''$. At angular scales smaller than $\approx 3''$, the fluctuations average out, since the bulk of the data is at a much larger angular scale. The field of view of the primary beam limits any sensitivity to CBR fluctuation at angular scales larger than about 200″.

The results over the relevant angular scale of the Owens Valley Radio Observatory (OVRO) North Celestial Pole experiment (Readhead et al. 1989) are also given in Figure 3. The OVRO NCP observations and these VLA observations have comparable sensitivity. At angular scales greater than 50″, the OVRO limits are lower, while the VLA results are more sensitive at smaller angular scales. These two experiments give a limit of $\Delta T/T_{CBR} < 4 \times 10^{-5}$ for Gaussian random fluctuations over $15'' < \theta_c < 500''$.

The limits from a previous VLA experiment at 4.9 GHz (Fomalont et al. 1988) are also shown in Figure 3. They are about a factor of 3 less accurate, except at coherence angles greater than about 120″. Most of the improvement is associated with our higher frequency, for which the brightness temperature sensitivity increases by $(8.44\ GHz/4.9\ GHz)^2 \approx 3.0$. The increased receiver sensitivity and the smaller contribution from background sources in the current VLA 8.44 GHz experiment are balanced by the increased integration time and the lower resolution in the previous 4.9 GHz experiment. In both VLA experiments the measurement of the CBR fluctuations is limited mostly by the system sensitivity, although the uncertainty in the surface density of weak foreground sources at microjansky levels adds significant errors at resolution less than 30″. Other experimental results are plotted in the figure at the angular scale which produces their best sensitivity. Extension to other angular scales would follow a similar form to that of the curves presented for the other experiments.

The limits to fluctuations of circularly polarized and linearly polarized emission are comparable to those for the total intensity. Since these data were of the same quality but less contaminated by foreground radio sources (which are not highly polarized), the limits are somewhat better than the total-intensity fluctuation limits at resolutions smaller than 30″.

6.3. *Comparison with Models*

A detailed comparison of models which predict CBR fluctuations at angular scales near 1′ has been given by Readhead et al. (1989, Table 6). However, with the recent detection of possible fluctuations at angular scales greater than $\sim 10°$ (Smoot et al. 1992) and recent advances in the knowledge of the large-scale structure of the universe (e.g., Ramella, Geller, & Huchra 1992), more sophisticated and predictive models should soon be generated. The observed *COBE* fluctuation level of $\Delta T/T_{CBR} = 1.1 \times 10^{-5}$, and its possible independence of angular scale, has given some impetus to "conventional" models tied to baryonic cold dark matter and a primordial power-law spectrum (Wright et al. 1992). The more unconventional models in which the underlying mass distribution is not strongly tied to the radiative distribution may not be so compelling.

However, any primordial brightness fluctuations of angular scale less than about 10′ are smoothed out during and after recombination, although the associated fluctuations in the underlying mass distribution may be the seeds around which galaxies and clusters were formed. In order to detect CBR fluctuations at arcminute scales, reionization must occur at redshifts $z < 10$, since fluctuations produced at an earlier epoch will blend away because of averaging in the line of sight, and by gravitational mixing during their propagation. Since quasars and other sources off ionizing radiation were probably not formed in sufficient quantity until $z \approx 4$, recent reionization is likely. Concomitant fluctuations in the CBR could be as small as 10″ for galaxy-sized volumes or tens of arcminutes for supercluster-sized volumes, and depend on the amount of ionizing radiation and the density of the cool material. Most modeling of the polarized emission of the CBR fluctuations suggests that the degree of linear polarization is about 10% (Bond & Efstathiou 1984). The circular polarization component should be less than a few percent of the unpolarized component.

[7] The 80″ image with a slightly lower $\Delta T/T$ contains only a small amount of data over a restricted range of angular scales. Its use does not produce more accurate results than the 60″ image.

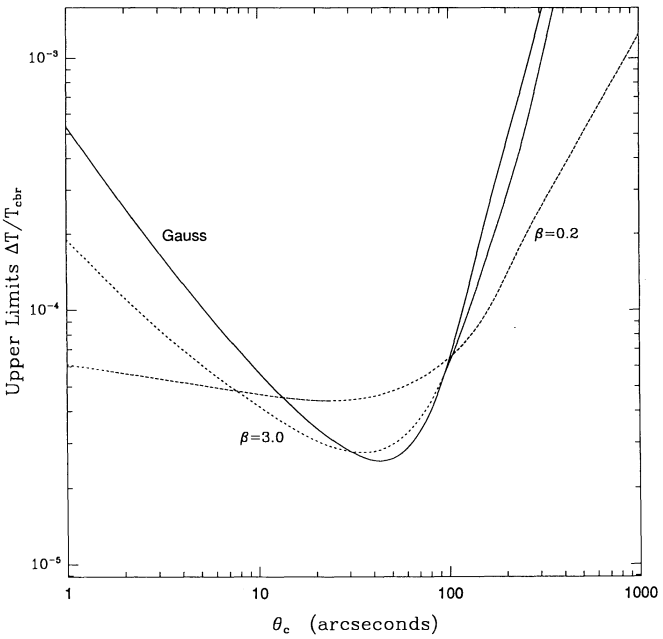

FIG. 4.—Limits to the CBR fluctuation models from the VLA 60″ image. The solid curve shows the limits for Gaussian fluctuations. The dashed curves show the limits for fluctuations with power-law exponents of 0.2 and 3.0.

Some models predict non-Gaussian fluctuations. Powerful explosions (Ostriker & Cowie 1981; Ikeuchi 1981) can produce blast waves which evacuate gas from a large area and can produce shell-like regions of galaxy formation and radiative fluctuations. If early galaxy formation and reionization are associated with cosmic strings, then fluctuations in the CBR will have a non-Gaussian fluctuation spectrum. Experiments which are designed to detect relatively large but spatially rare fluctuations in the CBR are important (e.g., Myers et al. 1993).

In Figure 4 we have compared the results of our observations to generic fluctuation models with different power spectra. The solid curve shows the results, also plotted in Figure 3, for Gaussian random fluctuations of coherence angle θ_c. For typical power-law fluctuation spectra, we used the form $C(\theta) = C_0[1 + (\theta/\theta_c)^2/2\beta]^{-\beta}$, $\beta > 0$ (Bond & Efstathiou 1984). It is similar to the one used by Holtzman (1989), but simpler. The curve for $\beta = 0.2$ simulates a fluctuation spectrum which is nearly independent of angular scale. The limits of $\Delta T/T$ are less than 1×10^{-4} between 0.″3–150″. The curve for $\beta = 3.0$ is similar to that for Gaussian fluctuations, reaching a minimum limit of 2.4×10^{-5} at $\theta_c = 40''$.

7. CONCLUSIONS

We have measured limits (95% confidence level) of Gaussian random fluctuations in the sky of $\Delta T/T_{\rm CBR} < 1.9 \times 10^{-5}$ at a resolution of 80″. These limits are the most accurate at these scales, and within a factor of 2 of the amplitude of the fluctuations recently detected by *COBE* at 10° angular scales. When combined with the OVRO NCP experiment, a limit of $\Delta T/T_{\rm CBR} < 3 \times 10^{-5}$ is obtained for Gaussian random fluctuations over the entire angular scale 15″–500″. Similar limits are obtained for linearly and circularly polarized fluctuations.

The most accurate limits to the CBR fluctuations from these observations were obtained between 40″ and 80″ resolution, where only 15% of the data were used. However, the higher resolution data with its good sensitivity to point sources was crucial in determining the surface density of sources down to 14.5 μJy in the field. With the extrapolation to lower flux densities, the contribution of fluctuations from weak foreground radio sources could be accurately estimated. The experimental results nearly reached the ultimate sensitivity limit of the observations given by the receiver noise, integration time, and bandwidth. Additional contributions from the uncertainty in the contribution from weak radio sources and from calibration and other errors are present but are less important than that from the receiver noise.

These results were obtained with less than 100 hr of integration time over a 15 day period. They are thus competitive with other experiments which have invested much more telescope time and special effort. Since the VLA is a highly versatile instrument, significantly longer blocks of time will, thus, be difficult to obtain. Observations at higher frequency with the VLA will decrease the foreground source contamination; however, the increased resolution makes CBR fluctuation results less interesting. At the present time, the lack of sensitivity of the VLA system at these high frequencies precludes serious observations even with the better brightness temperature sensitivity and less source contamination.

Since this experiment is limited mainly by receiver noise, further observations with the same configuration will improve in rms sensitivity with the square root of time. With 62 hr of integration on the Lynx field we obtained a limit of 1.9×10^{-5}. With about 400 hr of integration time, the rms sensitivity would be 4×10^{-6} and the 95% confidence level for no detection would be 7×10^{-6}. However, the removal of the discrete sources might be more of a limitation than for this experiment, where about 10% of the 10″ resolution image was contaminated by sources. With a factor of 2.5 increase in sensitivity, approximately 30% of the image area will be within 10″ of a detected source above 5.8 μJy. The tentative upgrading of the VLA in the future may significantly improve the VLA system (better receivers, wider bandwidth) so that the above sensitivity limit can be obtained in a reasonable amount of integration time.

We thank Craig Hogan and Ravi Sheth for their help in the analysis of the data. R. A. W. was supported by NSF grant AST-8821016 and the Alfred P. Sloan Foundation. R. B. P. was supported by NSF grant AST-8914988.

APPENDIX

Following the analysis of Readhead et al. (1989), we have determined the relationship between the image variance and the sky variance using the dirty-beam and primary-beam patterns. First, the relationship between the sky emission and the image response is given by the convolution

$$I(\vec{x}) = \int_{\vec{z}} T(\vec{x})B(\vec{x} - \vec{z})d\vec{z}\ , \qquad \text{(A1)}$$

where $\bar{z}$, $\bar{x}$ give the location in the sky or image, $T(\bar{x})$ is the sky emission, $I(\bar{x})$ is the image response, and $B(\bar{x})$ is the dirty beam multiplied by the primary-beam attenuation pattern. If the sky emission is dominated by pseudorandom fluctuations, the statistical nature of the emission can be described by the two-point coherence function $C_{\rm sky}(\bar{x})$, which is defined by

$$C_{\rm sky}(\bar{x}) = \int_{\bar{z}} T(\bar{z})T(\bar{z} - \bar{x})d\bar{z} \, . \tag{A2}$$

It is often assumed to have Gaussian form with variance C_0 and correlation length θ_c.

$$C_{\rm sky}(|\,\bar{x}\,|) = C_0 \exp\left(-\frac{\bar{x}^2}{2\theta_c^2}\right). \tag{A3}$$

The resulting two-point coherence function observed in the image, $C_{\rm obs}(\bar{x})$, is the triple convolution

$$C_{\rm obs}(\bar{x}) = C_{\rm sky}(\bar{x}) * B(\bar{x}) * B(\bar{x}) \, . \tag{A4}$$

The image variance is simply $C_{\rm obs}(0)$. The convolutions can be avoided by transforming the above equation into the Fourier domain, to obtain

$$C_{\rm obs}(0) = \int_{\bar{x}} F^2\{B(\bar{x})\}F\{C_{\rm sky}(\bar{x})\}d\bar{x} \, , \tag{A5}$$

where F denotes a Fourier transform. Notice that the square of the Fourier transform of the dirty beam is just the sampling distribution of the aperture (u-v coverage) and measures the relative power sensitivity of the observations as a function of angular frequency. The Fourier transform of the coherence function is the angular power spectrum of the fluctuations in the sky. Thus, the integral of the product of these two distributions is the proportion of the angular power in the sky fluctuations which are intercepted by the aperture to produce the image fluctuations.

A simple interpretation of the above equation is the following: If the full width at half-power resolution of the image is $\theta_{\rm FWHP}$, then power with coherence angles $\theta_c > \theta_{\rm FWHP}/2.3$ is intercepted by the array. The factor of 2.3 comes from the different definition used for the coherence length (one-sided 61% level) and the full width at half-maximum (two-sided 50% level). No power is obtained, however, for coherence angles larger than the field of view of the primary beam, $\theta_{\rm pb}$. The maximum sensitivity to fluctuations in the sky is obtained at a correlation angle somewhere near $(\theta_{\rm FWHM}\,\theta_{\rm pb})^{1/2}/2.3$.

REFERENCES

Aizu, K., Inoue, M., & Tabara, H. 1987, in IAU Symp. 124, Observational Cosmology, ed. A. Hewitt, G. Burbidge, & L. Z. Fang (Dordrecht: Reidel), 565
Altschuler, R., & Wardle, J. F. C. 1976, MemRAS, 82, 1
Baars, J. W. M., Genzel, R., Pauliny-Toth, I. I. K., & Witzel, A. 1977, A&A, 61, 99
Bond, J. R. 1988, in The Early Universe, ed. W. G. Unruh & G. W. Semenoff (Dordrecht: Reidel), 283
Bond, J. R., Carr, B. J., & Hogan, C. J. 1991, ApJ, 367, 420
Bond, J. R., & Efstathiou, G. 1984, ApJ, 285, L45
———. 1987, MNRAS, 226, 655
Davies, R. D., Lasenby, A. N., Watson, R. A., Daintree, E. J., Hopkins, J., Beckman, J., Almeida-Sanchez, J., & Rebolo, R. 1987, Nature, 326, 462
Donnelly, R. H., Partridge, R. B., & Windhorst, R. A. 1987, ApJ, 321, 94
Fomalont, E. B., Kellermann, K. I., Anderson, M. C., Weistrop, D., Wall, J. V., Windhorst, R. A., & Kristian, J. A. 1988, AJ, 96, 1187
Fomalont, E. B., Kellermann, K. I., Wall, J. V., & Weistrop, D. 1984, Science, 225, 23
Fomalont, E. B., Windhorst, R. A., Kristian, J. A., & Kellermann, K. I. 1991, AJ, 102, 1258
Franceschini, A., Toffolatti, L., Danese, L., & De Zotti, G. 1989, ApJ, 344, 35
Högbom, J. A. 1974, A&AS, 15, 417
Hogan, C. J., & Partridge, R. B. 1989, ApJ, 341, L29
Holtzman, J. A. 1989, ApJS, 71, 1
Ikeuchi, S. 1981, PASJ, 33, 211
Kaiser, N., & Silk, N. 1986, Nature, 324, 529
Kreysa, E., & Chini, A. 1989, in Proc. Third ESO/CERN Meeting, Astronomy: Cosmology and Fundamental Physics, ed. M. Caffo, R. Fanti, G. Giacomelli, & A. Renzini (Dordrecht: Kluwer), 433
Lang, K. R. 1980, Astrophysical Formulae (New York: Springer-Verlag)
Martin, H. M., & Partridge, R. B. 1988, ApJ, 324, 794
Meinhold, P., & Lubin, P. 1991, ApJ, 370, L11
Meyer, S. S., Cheng, E. S., & Page, L. K. 1991, ApJ, 371, L7
Myers, S. T., Readhead, A. C. S., & Lawrence, C. R. 1993, ApJ, in press
Oort, M. J. A., & Windhorst, R. A. 1985, A&A, 145, 405
Ostriker, J. P., & Cowie, L. L. 1981, ApJ, 243, L127
Ostriker, J. P., & Vishniac, E. T. 1986, ApJ, 306, L51
Partridge, R. B. 1988, Rep. Prog. Phys., 51, 647
Ramella, M., Geller, M. J., & Huchra, J. P. 1992, ApJ, 384, 396
Readhead, A. C. S., Lawrence, C. R., Myers, S. T., Sargent, W. L. W., Hardebeck, H. E., & Moffet, A. T. 1989, ApJ, 346, 566
Sachs, R. K., & Wolfe, A. M. 1967, ApJ, 353, 149
Schwarz, U. J. 1978, A&A, 65, 345
Smoot, G. F., et al. 1992, 396, L1
Timbie, P. T., & Wilkinson, D. T. 1990, ApJ, 353, 149
Uson, J. M., & Wilkinson, D. T. 1984, ApJ, 277, L1
Vishniac, E. T. 1987, ApJ, 322, 597
Wilkinson, D. T. 1986, Science, 232, 1517
Windhorst, R. A., Fomalont, E. B., Partridge, R. B., & Lowenthal, J. D. 1993, ApJ, in press
Windhorst, R. A., Mathis, D. F., & Neuschaefer, L. W. 1990, in ASP Conf. Ser., Vol. 10, Evolution of the Universe of Galaxies (Edwin Hubble Centennial Symposium), ed. R. G. Kron (Provo: BookCrafters, Inc.), 389
Windhorst, R. A., Miley, G. K., Owen, F. N., Kron, R. G., & Koo, D. C. 1985, ApJ, 289, 494
Wright, E. L., et al. 1992, 396, L13